Available online at www.sciencedirect.com
SCIENCE DIRECT®
Journal of Computational Physics 193 (2003) 21–39
JOURNAL OF COMPUTATIONAL PHYSICS
www.elsevier.com/locate/jcp

Adaptive biorthogonal spline schemes for advection–reaction equations

Richard E. Ewing [a,*], Jiangguo Liu [a], Hong Wang [b]

[a] *Institute for Scientific Computation, Texas A&M University, College Station, TX 77843-3404, USA*
[b] *Department of Mathematics, University of South Carolina, Columbia, SC 29208, USA*

Received 24 February 2003; received in revised form 25 June 2003; accepted 25 July 2003

Abstract

In this paper, based on Eulerian–Lagrangian localized adjoint method (ELLAM), we use biorthogonal spline wavelets to develop numerical schemes for multidimensional advection–reaction equations. The derived schemes produce accurate numerical solutions even if large time steps are used. These schemes are explicit but unconditionally stable. They also have the ability to carry out adaptive compression while preserving the total mass. Numerical experiments including observations on their convergence rates are presented to show the strong potential of these methods.

PACS: 65M25; 65M60; 76M25; 76S05

Keywords: Adaptive compression; Advection–reaction equations; Biorthogonal wavelets; Characteristic methods; Splines; Wavelet decomposition

1. Introduction

Advection–reaction partial differential equations arise from petroleum reservoir simulation, groundwater contaminant remediation, and many other applications. The solutions to these kinds of problems usually have moving steep fronts and cause serious numerical difficulties. Standard numerical methods produce either excessive nonphysical oscillations or extra numerical diffusion, which smears the steep fronts. Therefore, many special numerical techniques have been developed to overcome these difficulties. Among them, Eulerian–Lagrangian localized adjoint method (ELLAM) [2,14,20,21] is prominent. As a time-stepping procedure, it produces very accurate numerical solutions even if large time steps are used. ELLAM framework leaves many doors open in spatial aspects so finite element methods, finite volume

* Corresponding author. Present address: Texas A&M University, Office of the vice President for Research, Tamu 3404, USA.
E-mail address: richard_ewing@tamu.edu (R.E. Ewing).

0021-9991/$ - see front matter
doi:10.1016/j.jcp.2003.07.016

methods, and other new methods can be applied to spatial grids. Moreover, all boundary conditions are naturally incorporated into variational forms and mass is conserved.

In recent years, the localization capability and multilevel structure of wavelets have been utilized to develop efficient numerical methods for elliptic problems and conservation laws [1,4,6,12,13]. For advection-dominated problems, the existence of moving sharp fluid interfaces between smooth structures is a clear indication for application of wavelet techniques. In [22], we used orthogonal scaling functions and wavelets as trial and test functions within ELLAM framework to develop explicit but unconditionally stable schemes for advection–reaction equations. In this paper, we continue this effort and extend the ideas to biorthogonal spline wavelets. Spline functions will be used as trial functions to approximate the solution and a family of numerical schemes will be developed. These include the single level scheme using only scaling functions, the multilevel scheme using both scaling functions and wavelets, and the adaptive multilevel scheme that can carry out mass-conservative compression. These biorthogonal spline schemes possess some features of traditional finite element methods besides the advantages of adaptivity.

We organize the rest of this paper as follows: In Section 2, the main ideas of ELLAM framework are reviewed through the derivation of a reference equation for the initial value problem of multidimensional advection–reaction equations. Then we outline the basic theory about multiresolution analyses (MRA), orthogonal wavelets, and biorthogonal wavelets in Section 3. Section 4 is dedicated to the development of explicit but unconditionally stable numerical schemes based on biorthogonal spline wavelets. Then in Section 5 we present some numerical results and observe the convergence rates of these numerical schemes. Finally in Section 6 we make some remarks and discussions.

2. An Eulerian–Lagrangian weak formulation

We consider the following initial value problem to linear advection–reaction equation in multidimensional spaces:

$$\begin{cases} u_t + \nabla \cdot (\mathbf{V}u) + Ru = f(\mathbf{x},t), & (\mathbf{x},t) \in \mathbb{R}^d \times [0,T], \\ u(\mathbf{x},0) = u_0(\mathbf{x}), & \mathbf{x} \in \mathbb{R}^d, \end{cases} \tag{1}$$

where $u(\mathbf{x},t)$ is the unknown concentration function, $\mathbf{V}(\mathbf{x},t)$ represents a fluid velocity field, $R(\mathbf{x},t)$ is a first order reaction coefficient, $f(\mathbf{x},t)$ is a source/sink term, and $u_0(\mathbf{x})$ is a prescribed initial condition. We assume that $u_0(\mathbf{x})$ and $f(\mathbf{x},t)$ are compactly supported, hence so is the exact solution $u(\mathbf{x},t)$ for any finite time.

Let $0 = t_0 < t_1 < \cdots < t_{n-1} < t_n < \cdots < t_N = T$ be a partition of $[0,T]$ with $\Delta t_n := t_n - t_{n-1}$. We choose the test function $w(\mathbf{x},t)$ in such a way that it vanishes outside the space-time strip $\mathbb{R}^d \times (t_{n-1}, t_n]$ and is discontinuous in time at time t_{n-1}. Then integration by parts yields the following weak formulation [2,15,16]

$$\begin{aligned} &\int_{\mathbb{R}^d} u(\mathbf{x},t_n) w(\mathbf{x},t_n)\,\mathrm{d}\mathbf{x} - \int_{t_{n-1}}^{t_n} \int_{\mathbb{R}^d} (u(w_t + \mathbf{V}\cdot\nabla w - Rw))(\mathbf{x},t)\,\mathrm{d}\mathbf{x}\,\mathrm{d}t \\ &\quad = \int_{\mathbb{R}^d} u(\mathbf{x},t_{n-1}) w\big(\mathbf{x},t_{n-1}^+\big)\,\mathrm{d}\mathbf{x} + \int_{t_{n-1}}^{t_n} \int_{\mathbb{R}^d} f(\mathbf{x},t) w(\mathbf{x},t)\,\mathrm{d}\mathbf{x}\,\mathrm{d}t, \end{aligned} \tag{2}$$

where $w(\mathbf{x},t_{n-1}^+) := \lim_{t \to t_{n-1}^+} w(\mathbf{x},t)$ takes into account the fact that $w(\mathbf{x},t)$ is discontinuous in time at time t_{n-1}.

To develop an efficient numerical scheme reflecting the hyperbolic nature of the problem, we are motivated by the ideas of ELLAM [2] to eliminate the second term on the left side. This means the test function should satisfy the following *adjoint equation*

$$w_t + \mathbf{V}\cdot\nabla w - Rw = 0. \tag{3}$$

Note that the *characteristic* $\mathbf{y}(s;\mathbf{x},t)$ passing through $(\mathbf{x},t)$ is determined by the following initial value problem of ordinary differential equation (ODE):

$$\begin{cases} \frac{\mathrm{d}\mathbf{y}}{\mathrm{d}s} = \mathbf{V}(\mathbf{y},s), \\ \mathbf{y}(s;\mathbf{x},t)|_{s=t} = \mathbf{x}. \end{cases} \tag{4}$$

Along characteristics, the adjoint Eq. (3) becomes an ODE

$$\begin{cases} \frac{\mathrm{d}}{\mathrm{d}s} w(\mathbf{y}(s;\mathbf{x},t),s) - R(\mathbf{y}(s;\mathbf{x},t),s)\, w(\mathbf{y}(s;\mathbf{x},t),s) = 0, \\ w(\mathbf{y}(s;\mathbf{x},t),s)|_{s=t} = w(\mathbf{x},t). \end{cases} \tag{5}$$

Solving the problem gives us the following expression for the test function

$$w(\mathbf{y}(s;\mathbf{x},t),s) = w(\mathbf{x},t)\, e^{-\int_s^t R(\mathbf{y}(r;\mathbf{x},t),r)\,\mathrm{d}r}, \quad s\in[t_{n-1},t]. \tag{6}$$

Therefore, once the test function $w(\mathbf{x},t)$ is specified at time t_n, it is completely determined in the space-time strip $\mathbb{R}^d\times[t_{n-1},t_n]$ with exponential decay/growth along characteristic $\mathbf{y}(s;\mathbf{x},t_n)$ for $s\in[t_{n-1},t_n]$. If there is no reaction, then the test function is a constant on each characteristic.

Exact characteristic tracking is always preferred in numerical schemes whenever it is possible. Generally, we employ the Runge–Kutta method to approximate characteristics and use the following approximate test function instead:

$$w(\mathbf{y}(s;\mathbf{x},t_n),s) = w(\mathbf{x},t_n)e^{-R(\mathbf{x},t_n)(t_n-s)}, \quad \mathbf{x}\in\mathbb{R}^d,\ \ s\in[t_{n-1},t_n]. \tag{7}$$

Next we utilize the above test function to approximate the second term (source term) on the right side of the weak formulation

$$\begin{aligned} \int_{t_{n-1}}^{t_n}\int_{\mathbb{R}^d} f(\mathbf{y},s)w(\mathbf{y},s)\,\mathrm{d}\mathbf{y}\,\mathrm{d}s &= \int_{\mathbb{R}^d}\int_{t_{n-1}}^{t_n} f(\mathbf{y}(s;\mathbf{x},t_n),s)\, w(\mathbf{y}(s;\mathbf{x},t_n),s)\, |\mathbf{J}(\mathbf{y}(s;\mathbf{x},t_n),\mathbf{x})|\,\mathrm{d}s\,\mathrm{d}\mathbf{x} \\ &= \int_{\mathbb{R}^d} f(\mathbf{x},t_n)w(\mathbf{x},t_n)\left[\int_{t_{n-1}}^{t_n} e^{-R(\mathbf{x},t_n)(t_n-s)}\,\mathrm{d}s\right]\mathrm{d}\mathbf{x} + E(f,w) \\ &= \int_{\mathbb{R}^d} G(\mathbf{x},t_n)f(\mathbf{x},t_n)w(\mathbf{x},t_n)\,\mathrm{d}\mathbf{x} + E(f,w), \end{aligned} \tag{8}$$

where $\mathbf{J}$ is the Jacobian of $\mathbf{y}$ with respect to $\mathbf{x}$,

$$G(\mathbf{x},t_n) := \begin{cases} \Delta t_n & \text{if } R(\mathbf{x},t_n)=0, \\ \frac{1-e^{-R(\mathbf{x},t_n)\Delta t_n}}{R(\mathbf{x},t_n)} & \text{if } R(\mathbf{x},t_n)\neq 0, \end{cases} \tag{9}$$

and the truncation error

$$E(f,w) := \int_{\mathbb{R}^d}\int_{t_{n-1}}^{t_n} w(\mathbf{x},t_n)e^{-R(\mathbf{x},t_n)(t_n-s)} \quad [f(\mathbf{y}(s;\mathbf{x},t_n),s)|\mathbf{J}(\mathbf{y}(s;\mathbf{x},t_n),\mathbf{x})| - f(\mathbf{x},t_n)]\,\mathrm{d}s\,\mathrm{d}\mathbf{x}.$$

Substituting Eq. (8) into Eq. (2) and dropping the error term gives us a reference equation

$$\int_{\mathbb{R}^d} u(\mathbf{x},t_n)w(\mathbf{x},t_n)\,\mathrm{d}\mathbf{x} = \int_{\mathbb{R}^d} u(\mathbf{x},t_{n-1})w\big(\mathbf{x},t_{n-1}^+\big)\,\mathrm{d}\mathbf{x} + \int_{\mathbb{R}^d} G(\mathbf{x},t_n)f(\mathbf{x},t_n)w(\mathbf{x},t_n)\,\mathrm{d}\mathbf{x}. \tag{10}$$

3. Multiresolution analyses and wavelets

In Fourier analysis, L^2-functions are represented as linear combinations of sines and cosines. In 1910, Haar studied the representation of L^2-functions by step functions taking values ± 1 [11]. In the 1980s and 1990s, these ideas were explored further and developed into the theory of wavelets. Multiresolution analysis, as one of the most sophisticated ways of constructing wavelets, was introduced by Mallat from the image processing field into mathematics [17]. Compactly supported wavelets with arbitrary regularity were devised by Daubechies [8]. Wavelet analysis has proved to be an efficient tool in approximation theory and for capturing local and transient phenomena [9,10,18,19].

3.1. Multiresolution analyses, scaling functions and orthogonal wavelets

An orthogonal wavelet is simply an L^2-function $\psi(x)$ with some oscillations and a zero average $\int_{\mathbb{R}} \psi(x)\,dx = 0$ such that its shifted dilates $\psi_{j,k}(x) := 2^{j/2}\psi(2^j x - k),\ j,k \in \mathbb{Z}$ form an orthonormal basis (ONB) of $L^2(\mathbb{R})$. Loosely speaking, wavelets are small waves with rapid decay or compact supports, and hence have good localization capability, whereas the sine and cosine used in Fourier analysis are harmonic waves spreading over the whole real line and lack the aforementioned capability.

Usually orthogonal wavelets are connected with MRA. An MRA is a sequence of closed subspaces in $L^2(\mathbb{R})$ satisfying

(i) $V_j \subset V_{j+1}, \forall j \in \mathbb{Z}$, $\bigcap_{j\in\mathbb{Z}} V_j = \{0\}$, $\overline{\bigcup_{j\in\mathbb{Z}} V_j} = L^2(\mathbb{R})$ (completeness);
(ii) $f(\cdot) \in V_j \Longleftrightarrow f(2^{-j}\cdot) \in V_0$, $\forall j \in \mathbb{Z}$ (dilation invariance);
(iii) $f \in V_0 \Rightarrow f(\cdot - k) \in V_0$, $\forall k \in \mathbb{Z}$ (translation invariance);
(iv) $\exists \phi \in V_0$, called *scaling function*, so that $\{\phi_{0,k} \,|\, k \in \mathbb{Z}\}$ is an ONB of V_0, where $\phi_{j,k}(x) := 2^{j/2}\phi(2^j x - k),\ j,k \in \mathbb{Z}$.

By dilation invariance, $\{\phi_{j,k} \,|\, k \in \mathbb{Z}\}$ is also an ONB of V_j. Any $f \in L^2(\mathbb{R})$ can be approximated by its orthogonal projection onto V_j

$$P_j f := \sum_{k\in\mathbb{Z}} \langle f, \phi_{j,k}\rangle \phi_{j,k}. \tag{11}$$

Then the completeness implies convergence $\lim_{j\to\infty} \|P_j f - f\|_{L^2} = 0$.

Let W_0 be the orthogonal complement of V_0 in V_1, that is,

$$V_1 = V_0 \oplus W_0, \tag{12}$$

then there exists an orthogonal wavelet $\psi(x)$ such that $\{\psi_{0,k} \,|\, k \in \mathbb{Z}\}$ is an ONB of W_0. Accordingly, $\{\psi_{j,k} \,|\, k \in \mathbb{Z}\}$ is an ONB of W_j and

$$V_{j+1} = V_j \oplus W_j. \tag{13}$$

Let $Q_j : L^2(\mathbb{R}) \to W_j$ be the orthogonal projection defined by

$$Q_j f := \sum_{k\in\mathbb{Z}} \langle f, \psi_{j,k}\rangle \psi_{j,k}. \tag{14}$$

Then by Eq. (13), we have

$$P_{j+1} f = P_j f + Q_j f. \tag{15}$$

Obviously, $P_{j+1}f$ approximates f at a finer scale than $P_j f$ does. In other words, $P_{j+1}f$ reveals more details, which are represented by the wavelet terms in $Q_j f$.

Since $\phi \in V_0 \subset V_1$ and $\{\phi_{1,k} \,|\, k \in \mathbb{Z}\}$ is an ONB of V_1, there exists a sequence of numbers $h = \langle h_n \rangle_{n\in\mathbb{Z}}$, called *filter*, such that

$$\phi = \sum_{n\in\mathbb{Z}} h_n \phi_{1,n}. \tag{16}$$

Similarly, from $\psi \in V_0 \subset V_1$, we have another filter $g = \langle g_n \rangle_{n\in\mathbb{Z}}$ such that

$$\psi = \sum_{n\in\mathbb{Z}} g_n \phi_{1,n}. \tag{17}$$

A permissible choice is $g_n = (-1)^n h_{1-n}$.
From Eq. (16), we have

$$\begin{aligned}\phi_{j,k}(x) &= 2^{j/2}\phi(2^j x - k) = 2^{j/2}\sum_n h_n \phi_{1,n}(2^j x - k) = \sum_n h_n 2^{(j+1)/2}\phi(2(2^j x - k) - n) \\ &= \sum_n h_n 2^{(j+1)/2}\phi(2^{j+1}x - (2k+n)).\end{aligned}$$

Let $l = 2k + n$, then $n = l - 2k$ and we obtain

$$\phi_{j,k}(x) = \sum_l h_{l-2k}\phi_{j+1,l}(x). \tag{18}$$

Similarly,

$$\psi_{j,k}(x) = \sum_l g_{l-2k}\phi_{j+1,l}(x). \tag{19}$$

Let $\alpha_{j,k} = \langle f, \phi_{j,k}\rangle$ and $\beta_{j,k} = \langle f, \psi_{j,k}\rangle$, then Eqs. (18) and (19) lead us to the following decomposition algorithm connecting coefficients of successive approximations:

$$\alpha_{j,k} = \sum_l h_{l-2k}\ \alpha_{j+1,k}, \quad \beta_{j,k} = \sum_l g_{l-2k}\ \alpha_{j+1,k}. \tag{20}$$

Moreover, Eqs. (18), (19) and orthogonality imply that $\langle \phi_{j,l}, \phi_{j+1,k}\rangle = h_{k-2l}$ and $\langle \psi_{j,l}, \phi_{j+1,k}\rangle = g_{k-2l}$. Then applying the definition of orthogonal projection and Eq. (15) gives the reconstruction algorithm

$$\begin{aligned}\alpha_{j+1,k} &= \langle f, \phi_{j+1,k}\rangle = \langle P_{j+1}f, \phi_{j+1,k}\rangle = \langle P_j f, \phi_{j+1,k}\rangle + \langle Q_j f, \phi_{j+1,k}\rangle \\ &= \sum_l \alpha_{j,l}\langle \phi_{j,l}, \phi_{j+1,k}\rangle + \sum_l \beta_{j,l}\langle \psi_{j,l}, \phi_{j+1,k}\rangle = \sum_l h_{k-2l}\alpha_{j,l} + \sum_l g_{k-2l}\beta_{j,l}.\end{aligned} \tag{21}$$

Let $J_c < J_f$ be the chosen coarsest and finest resolution levels, then applying Eqs. (13) and (15) recursively yields

$$V_{J_f} = V_{J_c} \oplus W_{J_c} \oplus \cdots \oplus W_{J_f - 1}, \tag{22}$$

and

$$f \approx \sum_k \langle f, \phi_{J_f,k}\rangle \phi_{J_f,k} = \sum_k \langle f, \phi_{J_c,k}\rangle \phi_{J_c,k} + \sum_{j=J_c}^{J_f-1}\sum_k \langle f, \psi_{j,k}\rangle \psi_{j,k}. \tag{23}$$

This motivates us to carry out a progressive/multilevel approximation. We first approximate the function from a coarse level, and then add in more details level by level through wavelet terms if necessary. In

addition, wavelet coefficients in the smooth regions of a function will be small and thus can be neglected to save computations and storage. In other words, compression in the wavelet decomposition can be performed to improve the efficiency of approximation.

The properties of the scaling function and wavelet used affect the performance of approximation in various aspects. The lengths of their supports determine computational cost. The number of vanishing moments of the wavelet implies compression potential. Given the number of vanishing moments, Daubechies' wavelets [8] have the minimal support length. In this aspect, they are optimal and hence popular in applications.

3.2. Biorthogonal wavelets

Biorthogonal wavelets were motivated by concerns about exact reconstruction and symmetry in signal processing, and developed to improve the shortcomings of orthogonal wavelets while maintaining their advantages [5]. Rather than one orthogonal wavelet and one orthogonal scaling function, two wavelets and two scaling functions satisfying the so-called biorthogonal relation are constructed. One remarkable feature is that, as we shall see later, the desired properties of vanishing moments and regularity are separated into two biorthogonal wavelets, and this separation proves to be very useful for many applications.

Applications of biorthogonal wavelets in sciences and engineerings have gone beyond signal processing or image processing. In numerical solutions for PDEs, they serve in an analogous capacity as Petrov–Galerkin methods do for finite element methods.

Now we construct biorthogonal wavelets and scaling functions from two pairs of filters (h, g) and $(\tilde{h}, \tilde{g})$ through two-scale equations:

$$\phi = \sum_{k\in\mathbb{Z}} h_k \phi_{1,k}, \quad \psi = \sum_{k\in\mathbb{Z}} g_k \phi_{1,k}, \quad \tilde{\phi} = \sum_{k\in\mathbb{Z}} \tilde{h}_k \tilde{\phi}_{1,k}, \quad \tilde{\psi} = \sum_{k\in\mathbb{Z}} \tilde{g}_k \tilde{\phi}_{1,k}. \tag{24}$$

The filters should satisfy the following condition

$$\overline{\hat{h}(\omega)}\,\hat{\tilde{h}}(\omega) + \overline{\hat{h}(\omega+\pi)}\,\hat{\tilde{h}}(\omega+\pi) = 2, \tag{25}$$

where $\hat{h}(\omega) := \sum_{n\in\mathbb{Z}} h_n e^{-in\omega}$ and similarly for $\hat{\tilde{h}}(\omega)$. Again permissible choices for g and $\tilde{g}$ are

$$g_n = (-1)^n \tilde{h}_{1-n}, \quad \tilde{g}_n = (-1)^n h_{1-n}. \tag{26}$$

Usually ϕ, ψ are called primal scaling function and wavelet, and $\tilde{\phi}, \tilde{\psi}$ are called dual scaling function and wavelet. But the roles of these two pairs of filters are symmetric and can be switched. Hence the same is true for the primals and duals.

Under certain conditions on the filters, $\{\psi_{j,k} \,|\, j,k \in \mathbb{Z}\}$ and $\{\tilde{\psi}_{j,k} \,|\, j,k \in \mathbb{Z}\}$ form two Riesz bases of $L^2(\mathbb{R})$. Namely, there exist two positive constants A and B such that for any $f \in L^2(\mathbb{R})$,

$$A\|f\|^2_{L^2(\mathbb{R})} \leqslant \|\langle f, \psi_{j,k}\rangle\|_2^2 \leqslant B\|f\|^2_{L^2(\mathbb{R})}, \tag{27}$$

$$\frac{1}{B}\|f\|^2_{L^2(\mathbb{R})} \leqslant \|\langle f, \tilde{\psi}_{j,k}\rangle\|_2^2 \leqslant \frac{1}{A}\|f\|^2_{L^2(\mathbb{R})}. \tag{28}$$

More important is the following biorthogonal relation:

$$\langle \phi_{0,k}, \tilde{\phi}_{0,k'}\rangle = \delta_{k,k'}, \tag{29}$$

$$\langle \psi_{j,k}, \tilde{\psi}_{j',k'}\rangle = \delta_{j,j'}\delta_{k,k'}. \tag{30}$$

Let

$$\begin{aligned} V_j &= \mathrm{Span}\{\phi_{j,k} | k \in \mathbb{Z}\}, \quad W_j = \mathrm{Span}\{\psi_{j,k} | k \in \mathbb{Z}\}, \\ \tilde{V}_j &= \mathrm{Span}\{\tilde{\phi}_{j,k} \,|\, k \in \mathbb{Z}\}, \quad \tilde{W}_j = \mathrm{Span}\{\tilde{\psi}_{j,k} \,|\, k \in \mathbb{Z}\}. \end{aligned} \tag{31}$$

Then the two sequences $\langle V_j \rangle_{j\in\mathbb{Z}}$ and $\langle \tilde{V}_j \rangle_{j\in\mathbb{Z}}$ satisfy the first three conditions but not the fourth one in the definition of MRA discussed in Section 3. Now $\{\phi_{0,k} \mid k \in \mathbb{Z}\}$ is not an ONB in general, but merely a Riesz basis of V_0. However, we still call $\langle V_j \rangle_{j\in\mathbb{Z}}$ an MRA. The same is true for $\{\tilde{\phi}_{0,k} \,|\, k \in \mathbb{Z}\}$ and $\langle \tilde{V}_j \rangle_{j\in\mathbb{Z}}$. It is not a surprise that the following holds

$$V_{j+1} = V_j + W_j, \quad \tilde{V}_{j+1} = \tilde{V}_j + \tilde{W}_j. \tag{32}$$

The biorthogonality implies that W_j is not necessarily orthogonal to V_j but is to $\tilde{V}_j$, whereas $\tilde{W}_j$ is not necessarily orthogonal to $\tilde{V}_j$ but is to V_j. This way, the biorthogonality binds the two MRA into a giant "zipper" [9].

For any $f \in L^2(\mathbb{R})$, there exist two representations

$$f = \sum_{j,k\in\mathbb{Z}} \langle f, \tilde{\psi}_{j,k} \rangle \psi_{j,k} = \sum_{j,k\in\mathbb{Z}} \langle f, \psi_{j,k} \rangle \tilde{\psi}_{j,k}. \tag{33}$$

Either way, one biorthogonal wavelet is used in decomposition (coefficients) while the other one is used in reconstruction (basis functions). But we prefer the wavelet used for coefficients to have more vanishing moments and the other one used for basis functions to have better regularity. In the smooth regions of the function, the wavelet coefficients will be small and compression can be carried out. So more vanishing moments mean a higher compression potential. On the other hand, when a smooth wavelet is used for basis functions, the error added to the wavelet coefficients from compression or quantization will introduce a smooth error in the approximation. Therefore, the desired properties of vanishing moments and regularity are separated into two biorthogonal wavelets, and this separation proves to be useful for many applications.

Finally, it is apparent from the nestedness of subspaces and biorthogonality that

$$V_j \perp \tilde{W}_{j'}, \quad \tilde{V}_j \perp W_{j'}, \quad \text{for } j \leqslant j'.$$

Therefore, rather than using the infinite expansions in Eq. (33), one can choose a coarse resolution level J_c and a fine level $J_f (> J_c)$ to carry out one-level or multilevel approximations similar to the orthogonal case

$$f \approx \sum_k \langle f, \tilde{\phi}_{J_f,k} \rangle \phi_{J_f,k} = \sum_k \langle f, \tilde{\phi}_{J_c,k} \rangle \phi_{J_c,k} + \sum_{j=J_c}^{J_f-1} \sum_k \langle f, \tilde{\psi}_{j,k} \rangle \psi_{j,k}. \tag{34}$$

3.3. Biorthogonal spline wavelets

Most orthogonal scaling functions and wavelets do not have explicit expressions, which is an obvious shortcoming for their applications in some situations. In this sense, biorthogonal spline wavelets are appealing since the primal scaling function and wavelet are splines, and hence have explicit expressions and known regularities. Therefore, numerical methods built upon biorthogonal spline wavelets possess some features of the traditional finite element methods besides the advantage of a multilevel structure.

For $p \in \mathbb{N}$, we take the pth order B-spline centered at 0 or $1/2$ (upon the parity of p) as the primal scaling function ϕ. Clearly, ϕ is a piecewise polynomial of degree $p-1$ and is C^{p-2} across knots. The number of

vanishing moments $\tilde{p}$ of ψ is set as a free parameter so that a family of corresponding wavelets can be constructed. Then the duals $\tilde{\phi}$ and $\tilde{\psi}$ follow [5]. The dual wavelet $\tilde{\psi}$ has p vanishing moments. The regularity of $\tilde{\phi}$ and $\tilde{\psi}$ increase with $\tilde{p}$, even though an accurate measurement is not so obvious. These four functions are denoted together as $\mathrm{Bior}(p,\tilde{p})$.

For $p = 2$ and $\tilde{p} = 4$, the primal scaling function and wavelet are piecewise linear functions, whereas the primal scaling function and wavelet of $\mathrm{Bior}(4,4)$ are cubic splines. Their graphs are plotted below and will be used in our numerical experiments.

As we shall see in the following section, the application of the Lagrangian coordinates in an Eulerian–Lagrangian scheme requires evaluation of the trial functions at the foot of a backtracking characteristic, which could be any point. So trial functions similar to splines having explicit expressions are very attractive.

3.4. Multivariate biorthogonal spline wavelets

Multivariate biorthogonal spline (or general) wavelets can be constructed through tensor products. For ease of exposure, we start from one group of biorthogonal spline wavelets $\phi, \psi, \tilde{\phi}, \tilde{\psi}$ and their associated MRA $\langle V_j\rangle_{j\in\mathbb{Z}}$ and $\langle \tilde{V}_j\rangle_{j\in\mathbb{Z}}$. This is also enough for most applications.

Let $\hat{E} := \{0,1\}^d := \{\mathbf{e} = (e_1,\ldots,e_d) | e_l = 0,1\}$ be the set of vertices of the d-dimensional unit cube and $E := \hat{E} \setminus \{\mathbf{0}\}$. Let $\mathbf{x} = (x_1,\ldots,x_d) \in \mathbb{R}^d$, $j \in \mathbb{Z}$, and $\mathbf{k} = (k_1,\ldots,k_d) \in \mathbb{Z}^d$. Then we define

$$\Phi(\mathbf{x}) := \prod_{l=1}^{d} \phi(x_l), \quad \tilde{\Phi}(\mathbf{x}) := \prod_{l=1}^{d} \tilde{\phi}(x_l), \tag{35}$$

$$\Psi^{\mathbf{e}}(\mathbf{x}) := \prod_{l=1}^{d} (\phi(x_l))^{1-e_l} (\psi(x_l))^{e_l}, \tag{36}$$

$$\tilde{\Psi}^{\mathbf{e}}(\mathbf{x}) := \prod_{l=1}^{d} (\tilde{\phi}(x_l))^{1-e_l} (\tilde{\psi}(x_l))^{e_l}, \quad \mathbf{e} = (e_1,\ldots,e_d) \in E. \tag{37}$$

Furthermore, for $j \in \mathbb{Z}$, we define

$$\mathbf{V}_j := \bigotimes_{l=1}^{d} V_j, \quad \tilde{\mathbf{V}}_j := \bigotimes_{l=1}^{d} \tilde{V}_j \tag{38}$$

as the closed linear span in $L^2(\mathbb{R}^d)$ of all functions of the form $f^1(x_1)\cdots f^d(x_d)$ where $f^l \in V_j$ or $\tilde{V}_j$, respectively, for all $l = 1,\ldots,d$.

It can be verified that $\langle \mathbf{V}_j\rangle_{j\in\mathbb{Z}}$ and $\langle \tilde{\mathbf{V}}_j\rangle_{j\in\mathbb{Z}}$ form two MRA in $L^2(\mathbb{R}^d)$. Therefore $\{\Phi_{j,\mathbf{k}} : \mathbf{k} \in \mathbb{Z}^d\}$ and $\{\tilde{\Phi}_{j,\mathbf{k}} : \mathbf{k} \in \mathbb{Z}^d\}$ are Riesz bases of $\mathbf{V}_j$ and $\tilde{\mathbf{V}}_j$, respectively, where

$$\Phi_{j,\mathbf{k}}(x) := 2^{jd/2}\Phi(2^j\mathbf{x} - \mathbf{k}), \quad j \in \mathbb{Z}, \ \mathbf{k} \in \mathbb{Z}^d \tag{39}$$

and $\tilde{\Phi}_{j,\mathbf{k}}(x)$ is understood similarly.

4. Biorthogonal spline schemes

By choosing primal scaling functions/wavelets as trial functions and dual scalings/wavelets as test functions, we can extend all orthogonal schemes developed in [22] to the biorthogonal case. This is similar to the ideas in the Petrov–Galerkin finite element method. The trial functions and test functions are different, but they span two spaces of the same dimension and still produce a well-defined discrete algebraic

system. However we shall restrict ourselves to biorthogonal spline wavelets, even though almost every thing holds for more general biorthogonal wavelets.

Let $\Phi(\mathbf{x}), \Psi(\mathbf{x}), \tilde{\Phi}(\mathbf{x}), \tilde{\Psi}(\mathbf{x})$ be the multivariate biorthogonal splines. Let $J_c < J_f$ be the chosen coarsest and finest spatial resolution levels. For all j with $J_c \leqslant j \leqslant J_f$, we define

$$\Lambda_j = \{\mathbf{k} : \mathrm{supp}\Phi_{j,\mathbf{k}} \cap \Omega \neq \emptyset\}, \tag{40}$$

$$\Lambda_{j,\mathbf{e}} = \{\mathbf{k} : \mathrm{supp}\Psi^{\mathbf{e}}_{j,\mathbf{k}} \cap \Omega \neq \emptyset\}, \tag{41}$$

$$\mathscr{P}_j(\Omega) = \mathrm{Span}\{\Phi_{j,\mathbf{k}}(\mathbf{x}) : \mathbf{k} \in \Lambda_j\}, \tag{42}$$

$$\tilde{\mathscr{P}}_j(\Omega) = \mathrm{Span}\{\tilde{\Phi}_{j,\mathbf{k}}(\mathbf{x}) : \mathbf{k} \in \Lambda_j\}. \tag{43}$$

4.1. Scheme I: A single level scheme

Find $U(\mathbf{x}, t_n) \in \mathscr{P}_{J_f}(\Omega)$ with

$$U(\mathbf{x}, t_n) = \sum_{\mathbf{k}\in\Lambda_{J_f}} c^n_{J_f,\mathbf{k}} \Phi_{J_f,\mathbf{k}}(\mathbf{x}) \tag{44}$$

such that for any test function $w(\mathbf{x}, t_n) = \tilde{\Phi}_{J_f,\mathbf{k}}(\mathbf{x}) \in \tilde{\mathscr{P}}_{J_f}(\Omega)$ the following holds

$$\int_\Omega U(\mathbf{x}, t_n) w(\mathbf{x}, t_n)\,\mathrm{d}\mathbf{x} = \int_\Omega U(\mathbf{x}, t_{n-1}) w\big(\mathbf{x}, t^+_{n-1}\big)\,\mathrm{d}\mathbf{x} + \int_\Omega G(\mathbf{x}, t_n) f(\mathbf{x}, t_n) w(\mathbf{x}, t_n)\,\mathrm{d}\mathbf{x}.$$

The biorthogonality of scaling functions immediately implies that this is an *explicit* scheme and the coefficients are computed by (see Figs. 1 and 2)

$$c^n_{J_f,\mathbf{k}} = \int_\Omega U(\mathbf{x}, t_{n-1}) w\big(\mathbf{x}, t^+_{n-1}\big)\,\mathrm{d}\mathbf{x} + \int_\Omega G(\mathbf{x}, t_n) f(\mathbf{x}, t_n) \tilde{\Phi}_{J_f,\mathbf{k}}(\mathbf{x})\,\mathrm{d}\mathbf{x}. \tag{45}$$

4.2. Scheme II: a multilevel scheme

Find $U(\mathbf{x}, t_n) \in \mathscr{P}_{J_f}(\Omega)$ with

$$U(\mathbf{x}, t_n) = \sum_{\mathbf{k}\in\Lambda_{J_c}} c^n_{J_c,\mathbf{k}} \Phi_{J_c,\mathbf{k}}(\mathbf{x}) + \sum_{j=J_c}^{J_f-1} \sum_{\mathbf{k}\in\Lambda_{j,\mathbf{e}}} d^{n,\mathbf{e}}_{j,\mathbf{k}} \Psi^{\mathbf{e}}_{j,\mathbf{k}}(\mathbf{x}) \tag{46}$$

such that the reference equation holds for any test function $w(\mathbf{x}, t_n) \in \tilde{\mathscr{P}}_{J_f}(\Omega)$.

Scheme II is also an explicit scheme. We choose $w(\mathbf{x}, t_n) = \tilde{\Phi}_{J_c,\mathbf{k}}(\mathbf{x})$ or $\tilde{\Psi}^{\mathbf{e}}_{j,\mathbf{k}}(\mathbf{x})$ respectively, then the biorthogonality again gives

$$c^n_{J_c,\mathbf{k}} = \int_\Omega U(\mathbf{x}, t_{n-1}) w\big(\mathbf{x}, t^+_{n-1}\big)\,\mathrm{d}\mathbf{x} + \int_\Omega G(\mathbf{x}, t_n) f(\mathbf{x}, t_n) \tilde{\Phi}_{J_c,\mathbf{k}}(\mathbf{x})\,\mathrm{d}\mathbf{x}, \tag{47}$$

$$d^{n,\mathbf{e}}_{j,\mathbf{k}} = \int_\Omega U(\mathbf{x}, t_{n-1}) w\big(\mathbf{x}, t^+_{n-1}\big)\,\mathrm{d}\mathbf{x} + \int_\Omega G(\mathbf{x}, t_n) f(\mathbf{x}, t_n) \tilde{\Psi}^{\mathbf{e}}_{j,\mathbf{k}}(\mathbf{x})\,\mathrm{d}\mathbf{x}, \tag{48}$$

$J_c \leqslant j \leqslant J_f - 1.$

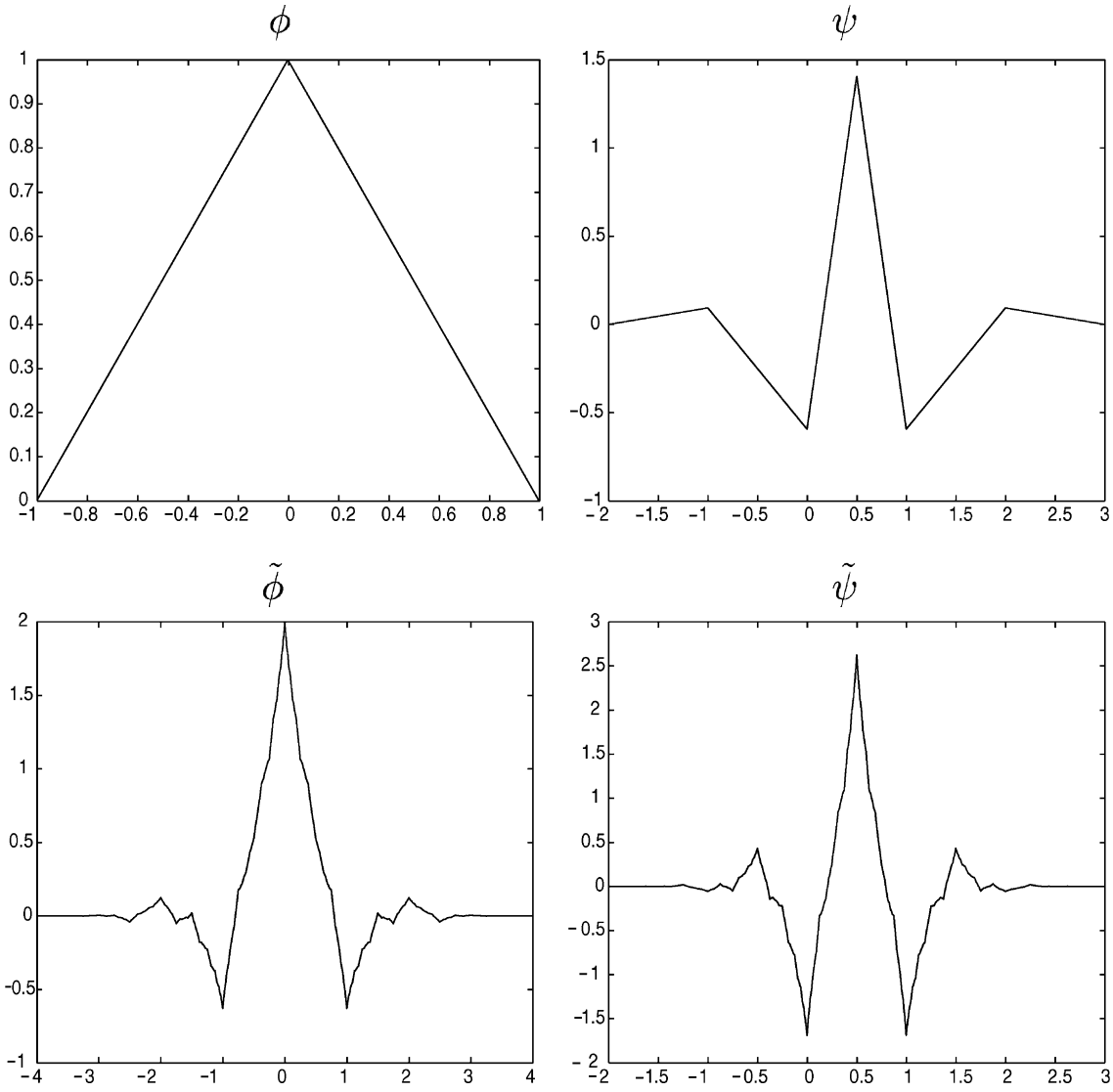

Fig. 1. Biorthogonal spline scaling functions and wavelets Bior(2, 4).

In Scheme II, the first part on the right side of Eq. (46) provides a basic approximation. As more finer terms in the second part come in, we obtain better approximations.

Theoretically, Scheme II is equivalent to Scheme I. But the wavelets used in Scheme II have the ability to localize singularities in the solution and the multilevel structure provides flexibility.

It is known in Fourier analysis that if a function is smooth then its Fourier coefficients decay rapidly. The same can be said about the biorthogonal wavelet coefficients of a function at its smooth parts. In applications, advection dominated transport equations often admit solutions with steep fronts within small regions but smooth outside these regions. While the decay properties of Fourier coefficients could be contaminated globally by local singularities of the function, biorthogonal wavelets can isolate these local singularities very well. So we are motivated to keep the terms in the wavelet expansion with noticeable coefficients that cor-

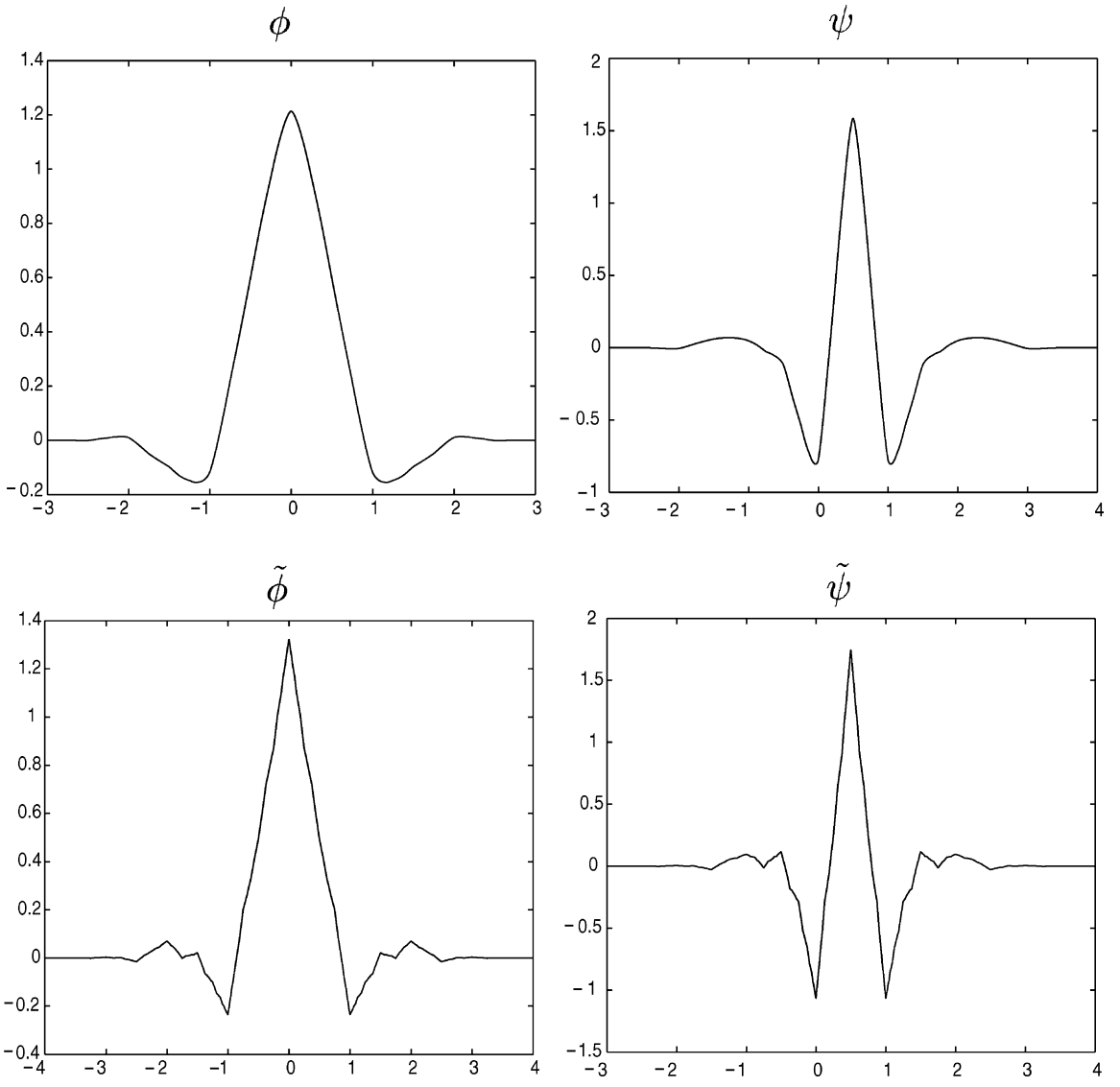

Fig. 2. Biorthogonal spline scaling functions and wavelets Bior(4, 4).

respond to the rough regions of the solution and to drop the terms with small coefficients that correspond to the smooth regions of the solution. Therefore, the number of unknowns to be solved will be reduced. In other words, we can develop a multilevel scheme with adaptive compression, which consists of 4 steps.

4.3. Scheme III: a multilevel scheme with adaptive compression

Step 1: Initialization. Project the initial data $u_0(\mathbf{x})$ into $\mathscr{P}_{J_f}(\Omega)$ to obtain its approximation

$$U(\mathbf{x}, t_0) = \sum_{\mathbf{k}\in\Lambda_{J_c}} c^0_{J_c,\mathbf{k}} \Phi_{J_c,\mathbf{k}}(\mathbf{x}) + \sum_{j=J_c}^{J_f-1} \sum_{\mathbf{e}\in E} \sum_{\mathbf{k}\in\Lambda_{j,\mathbf{e}}} d^{0,\mathbf{e}}_{j,\mathbf{k}} \Psi^{\mathbf{e}}_{j,\mathbf{k}}(\mathbf{x}) \tag{49}$$

with coefficients given by

$$c^0_{J_c,\mathbf{k}} = \int_\Omega u_0(\mathbf{x})\tilde{\Phi}_{J_c,\mathbf{k}}(\mathbf{x})\,d\mathbf{x}, \quad \mathbf{k} \in \Lambda_{J_c}, \tag{50}$$

$$d^{0,\mathbf{e}}_{j,\mathbf{k}} = \int_\Omega u_0(\mathbf{x})\tilde{\Psi}^{\mathbf{e}}_{j,\mathbf{k}}(\mathbf{x})\,d\mathbf{x}, \quad \mathbf{k} \in \Lambda_{j,\mathbf{e}},\ \mathbf{e} \in E,\ J_c \leqslant j \leqslant J_f - 1. \tag{51}$$

Step 2: Compression. At each time step $t_n, n = 0, 1, \ldots, N$, compress wavelet coefficients in the approximation

$$\hat{U}(\mathbf{x}, t_n) = \sum_{\mathbf{k}\in\Lambda_{J_c}} c^n_{J_c,\mathbf{k}}\Phi_{J_c,\mathbf{k}}(\mathbf{x}) + \sum_{j=J_c}^{J_f-1}\sum_{\mathbf{e}\in E}\sum_{\mathbf{k}\in\widehat{\Lambda^n_{j,\mathbf{e}}}} d^{n,\mathbf{e}}_{j,\mathbf{k}}\Psi^{\mathbf{e}}_{j,\mathbf{k}}(\mathbf{x}), \tag{52}$$

where $\widehat{\Lambda^n_{j,\mathbf{e}}}$ is the predicted significant coefficient index set with $\widehat{\Lambda^0_{j,\mathbf{e}}} := \Lambda_{j,\mathbf{e}}$ and $\widehat{\Lambda^n_{j,\mathbf{e}}}$ $(n = 1, \ldots, N)$ to be defined later.

First, we choose a threshold ε and define level-dependent thresholds by

$$\varepsilon_j := \varepsilon\, 2^{-(j-J_c)d/2}\Delta t[\|u_0\|_{L^2(\Omega)} + \|f\|_{L^2([0,T]\times\Omega)}]. \tag{53}$$

Then, we carry out the following thresholding process

$$\overline{d^{n,\mathbf{e}}_{j,\mathbf{k}}} := \begin{cases} d^{n,\mathbf{e}}_{j,\mathbf{k}} & \text{if } \left|d^{n,\mathbf{e}}_{j,\mathbf{k}}\right| \geqslant \varepsilon_j, \\ 0 & \text{otherwise.} \end{cases} \tag{54}$$

Next, we introduce the significant coefficient index sets

$$\overline{\Lambda^n_{j,\mathbf{e}}} := \left\{\mathbf{k} \in \widehat{\Lambda^n_{j,\mathbf{e}}} : \left|d^{n,\mathbf{e}}_{j,\mathbf{k}}\right| \geqslant \varepsilon_j\right\}. \tag{55}$$

Finally, a compression $\overline{U}(\mathbf{x}, t_n)$ of $\hat{U}(\mathbf{x}, t_n)$ is defined by

$$\overline{U}(\mathbf{x}, t_n) = \sum_{\mathbf{k}\in\Lambda_{J_c}} c^n_{J_c,\mathbf{k}}\Phi_{J_c,\mathbf{k}}(\mathbf{x}) + \sum_{j=J_c}^{J_f-1}\sum_{\mathbf{e}\in E}\sum_{\mathbf{k}\in\overline{\Lambda^n_{j,\mathbf{e}}}} d^{n,\mathbf{e}}_{j,\mathbf{k}}\Psi^{\mathbf{e}}_{j,\mathbf{k}}(\mathbf{x}). \tag{56}$$

Step 3: Prediction. In the above expansion, the scaling coefficients describe the size (scale) of the solution, while the biorthogonal wavelet coefficients depict the smoothness/roughness of the solution. The significant coefficient index sets $\overline{\Lambda^{n-1}_{j,\mathbf{e}}}$ indicate the smooth and rough regions of the solution $\hat{U}(\mathbf{x}, t_{n-1})$. Then we track $\overline{\Lambda^{n-1}_{j,\mathbf{e}}}$ forward along characteristics from time t_{n-1} to time t_n to obtain the predicted significant coefficient index sets $\widehat{\Lambda^n_{j,\mathbf{e}}}$.

Step 4: Solution. Once the predicted significant coefficient index sets $\widehat{\Lambda^n_{j,\mathbf{e}}}$ are determined, we define adaptive trial function subspace $\widehat{\mathscr{P}_{J_f}(\Omega)} \subset \mathscr{P}_{J_f}(\Omega)$ and adaptive test function subspace $\widehat{\tilde{\mathscr{P}}_{J_f}(\Omega)} \subset \tilde{\mathscr{P}}_{J_f}(\Omega)$, respectively by

$$\widehat{\mathscr{P}_{J_f}(\Omega)} := \mathrm{Span}\left\{\{\Phi_{J_c,\mathbf{k}}\}_{\mathbf{k}\in\Lambda^n_{J_c}}, \left\{\Psi^{\mathbf{e}}_{j,\mathbf{k}}\right\}_{\mathbf{k}\in\widehat{\Lambda^n_{j,\mathbf{e}}},\mathbf{e}\in E, J_c\leqslant j\leqslant J_f-1}\right\}, \tag{57}$$

$$\widehat{\tilde{\mathscr{P}}_{J_f}(\Omega)} := \mathrm{Span}\left\{\{\tilde{\Phi}_{J_c,\mathbf{k}}\}_{\mathbf{k}\in\Lambda^n_{J_c}}, \left\{\tilde{\Psi}^{\mathbf{e}}_{j,\mathbf{k}}\right\}_{\mathbf{k}\in\widehat{\Lambda^n_{j,\mathbf{e}}},\mathbf{e}\in E, J_c\leqslant j\leqslant J_f-1}\right\}. \tag{58}$$

Now we seek $\hat{U}(\mathbf{x}, t_n) \in \widehat{\mathscr{P}_{J_f}(\Omega)}$ with

$$\hat{U}(\mathbf{x}, t_n) = \sum_{\mathbf{k}\in\Lambda_{J_c}} c^n_{J_c,\mathbf{k}} \Phi_{J_c,\mathbf{k}}(\mathbf{x}) + \sum_{j=J_c}^{J_f-1} \sum_{\mathbf{e}\in E} \sum_{\mathbf{k}\in\widehat{\Lambda^n_{j,\mathbf{e}}}} d^{n,\mathbf{e}}_{j,\mathbf{k}} \Psi^{\mathbf{e}}_{j,\mathbf{k}}(\mathbf{x}) \tag{59}$$

such that for any $w(\mathbf{x}, t_n) \in \widehat{\tilde{\mathscr{P}}_{J_f}(\Omega)}$ the following holds

$$\int_\Omega \hat{U}(\mathbf{x}, t_n) w(\mathbf{x}, t_n)\,\mathrm{d}\mathbf{x} = \int_\Omega \overline{U}(\mathbf{x}, t_{n-1}) w(\mathbf{x}, t^+_{n-1})\,\mathrm{d}\mathbf{x} + \int_\Omega G(\mathbf{x}, t_n) f(\mathbf{x}, t_n) w(\mathbf{x}, t_n)\,\mathrm{d}\mathbf{x}. \tag{60}$$

Remark 1. The first part on the right side of (59) provides a basic approximation. The significant coefficients are nonzero only near the moving steep fronts, so the second part of the right side of (59) brings in progressive improvements in approximation. In this way, Scheme III resolves the moving steep fronts present in the solution accurately, adaptively, and efficiently.

Remark 2. We know that $U(\mathbf{x}, \cdot)$ represents concentration, so its integral is mass. The fact that the integral of a biorthogonal wavelet is zero guarantees that the compression performed in Scheme III preserves the total mass.

Remark 3. All three biorthogonal spline schemes are developed within the ELLAM framework, so they are not subject to the CFL restriction [7].

5. Numerical experiments

In this section, we present 1- (1D) and 2-dimensional (2D) numerical experiments on the biorthogonal spline wavelet schemes. We shall also observe their convergence rates and make brief comparison between solutions of biorthogonal wavelet schemes, orthogonal wavelet schemes proposed in [22], and traditional finite element methods.

5.1. Example 1: 1D sharp fronts

This is a linear advection problem with velocity field $V(x, t) = 1 + cx$, source term $f(x, t) = 0$, and initial condition

$$u_0(x) = \mathrm{erf}\left(\frac{x-a}{\sigma}\right) - \mathrm{erf}\left(\frac{x-b}{\sigma}\right), \tag{61}$$

where $\mathrm{erf}(x) = \int_{-\infty}^{x} e^{-y^2/2}\,\mathrm{d}y$. The exact solution is given by $u(x, t) = u_0(\xi)e^{-ct}$, where $\xi = [(1 + cx)e^{-ct} - 1]/c$ is obtained by backtracking characteristic from (x, t) to $(\xi, 0)$. Note that the initial solution has two sharp fronts located at $x = a$ and $x = b$, respectively. We expect the solution $u(x, t)$ at any time keeps these two sharp fronts.

In our numerical experiments, parameters are chosen as follows: $a = 0.25$, $b = 0.65$, $\sigma = 0.04$, and $c = 0.1$. For characteristic tracking, the second-order Runge–Kutta method is used.

Table 1 lists some numerical results of the three biorthogonal schemes with spline wavelets Bior$(4, 4)$ and different spatial resolutions and time steps. Trial functions are piecewise cubic polynomials. All three schemes generate very accurate numerical solutions even though large time steps and coarse spatial grids are used.

Table 1
Statistics of 1D schemes with Bior(4, 4)

Δt	J_c	J_f	Threshold ε	Max.	L^∞ error	L^2 error	L^1 error	Compr. ratio
Exact solution				0.9048	N/A			
0.1	7	7	N/A	0.9044	4.857E − 4	2.995E − 4	2.060E − 4	N/A
0.2	7	7	N/A	0.9039	1.419E − 3	6.590E − 4	4.652E − 4	N/A
0.2	6	6	N/A	0.9039	1.502E − 3	6.692E − 4	4.774E − 4	N/A
0.2	3	6	0	0.9040	2.337E − 3	7.993E − 4	5.807E − 4	N/A
0.2	3	6	1E − 3	0.9042	2.338E − 3	8.050E − 4	5.886E − 4	2.4
0.2	3	6	1E − 2	0.9055	4.587E − 3	1.502E − 3	9.845E − 4	3.1
0.2	3	6	5E − 2	0.9171	2.023E − 2	6.095E − 3	4.253E − 3	4.0
0.2	3	6	1E − 1	0.9300	6.833E − 2	2.105E − 2	1.516E − 2	4.8

The first 3 rows are results of Scheme I. They indicate that we have to refine both time step and spatial resolution in order to obtain better approximation. In some sense, Scheme I is equivalent to the traditional finite element method without local refinement.

As we know, Scheme II is a multilevel scheme and theoretically equivalent to the single level Scheme I. Numerically, there exist slight differences in their results. Of course, more interesting is the multilevel scheme with compression, i.e., Scheme III.

Generally speaking, the compression ratio of Scheme III increases as the threshold increases. We solve less unknowns and hence the scheme is more efficient. Meanwhile, the approximation deteriorates, as shown in the last 4 rows of Table 1. The best compression is no-compression, i.e., Scheme III with threshold 0, which is exactly Scheme II. The worst compression (a large threshold) will throw away all wavelet coefficients and give the result of Scheme I with the coarsest level. A good choice of the threshold in Scheme III, in other words, a quantitative description of trade-off between efficiency and accuracy related to compression, is a delicate issue of nonlinear approximation, and will be addressed in our future work.

For this particular problem, we have $\|u_0\|_{L^2(\Omega)} + \|f\|_{L^2([0,T]\times\Omega)} = 0.4$. Given $\varepsilon = 0.01$ as the threshold, Scheme III has compression ratio 3.1. This means we solve less than one-third of the original unknowns but still obtain very good approximation. Plots of uncompressed and compressed solutions with $J_c = 3, J_f = 6$ are shown in Fig. 3.

Next we conduct numerical experiments to observe the convergence rates in time and space. Our guess is that

$$\|U(x,T) - u(x,T)\|_{L^p(\Omega)} \leqslant M_\alpha(\Delta t)^\alpha + M_\beta h^\beta, \quad p = 1,2, \tag{62}$$

where $\alpha = 1$ and $\beta = 2$. We shall use linear regression to fit the constants in Eq. (62). First, we fix a small spatial step h and compute the constants α and M_α with respect to Δt. To measure the convergence rate in space, we choose different spatial steps h and time steps $\Delta t = Ch^2$ accordingly (for some fixed constant C). Tables 2 and 3 verify that our biorthogonal spline scheme possesses first-order accuracy in time and second-order accuracy in space. Notice that in the numerical experiments, M_α is much smaller than M_β. This reflects the fact that the solutions of advection–reaction equations are smoother along characteristics, and justifies the use of Lagrangian coordinates in the ELLAM methods. This also explains why we can still obtain very accurate numerical solutions even if large time steps are used, see Table 1.

5.2. Example 2: A 2D Gaussian pulse

In this example, the velocity field is posed as $V_1(x,y,t) = -4y$, $V_2(x,y,t) = 4x$, the reaction coefficient $R = \cos(2t)$, and the initial condition is given by

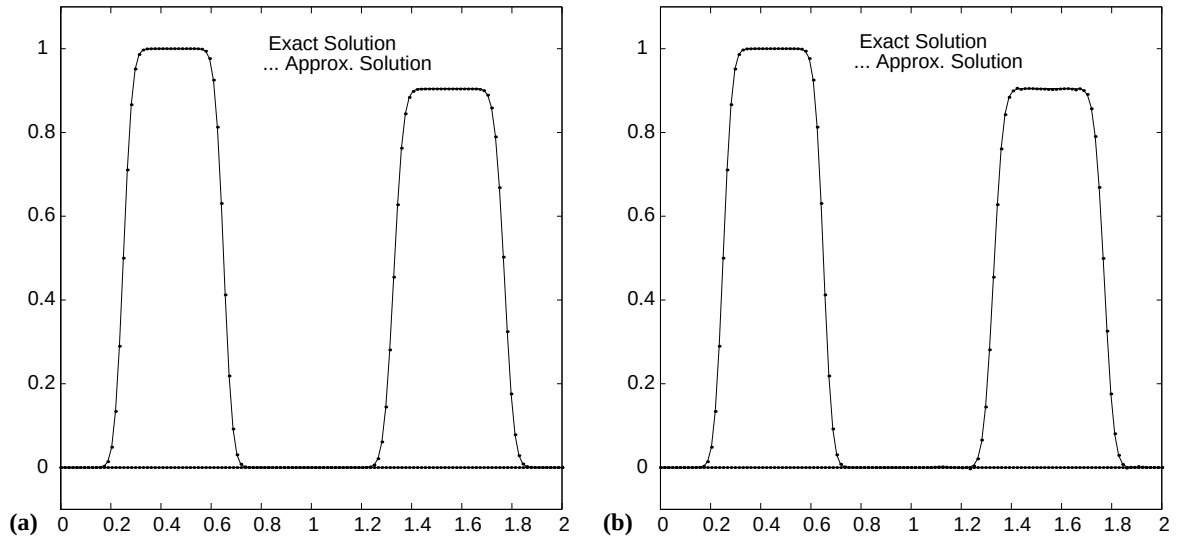

Fig. 3. 1D biorthogonal solutions with Bior(4, 4) and $\Delta t = 0.2$: (a) $J_c = J_f = 6$; (b) compressed $J_c = 3,\ J_f = 6,\ \varepsilon = 0.01$.

Table 2
Convergence rate in time, test for α and M_α

Δt	h	L^2 error	L^1 error
1/16	1/256	1.83518E − 4	1.26433E − 4
1/20	1/256	1.45988E − 4	1.00712E − 4
1/32	1/256	9.06279E − 5	6.27438E − 5
1/40	1/256	7.23697E − 5	5.01644E − 5
		$\alpha = 1.02$, $M_\alpha = 0.0031$	$\alpha = 1.01$, $M_\alpha = 0.0021$

Table 3
Convergence rate in space, test for β and M_β

h	Δt	L^2 error	L^1 error
1/64	1/5	6.69230E − 4	4.77369E − 4
1/128	1/20	1.45592E − 4	1.02097E − 4
1/256	1/80	3.60662E − 5	2.50861E − 5
1/512	1/320	9.01823E − 6	6.25288E − 6
		$\beta = 2.07$, $M_\beta = 3.4506$	$\beta = 2.08$, $M_\beta = 2.5937$

$$u_0(x,y) = \exp\left(-\frac{(x-x_c)^2 + (y-y_c)^2}{2\sigma^2}\right), \tag{63}$$

where (x_c, y_c) and σ are the center and standard deviation, respectively. If no source/sink is present, i.e., $f(x,y,t) \equiv 0$, then the analytical solution is given by

$$u(x,y,t) = \exp\left(-\frac{1}{2}\sin(2t) - \frac{(x_* - x_c)^2 + (y_* - y_c)^2}{2\sigma^2} \right), \tag{64}$$

where (x_*, y_*) is the backtracking image of (x, y) along characteristic from time t to time 0, that is, $x_* = (\cos 4t)x + (\sin 4t)y$, $y_* = -(\sin 4t)x + (\cos 4t)y$. The time interval is chosen as $[0, T] = [0, \pi/2]$, which is needed for one complete rotation. So the solution at the final time $T = \pi/2$ is identical to the initial condition, which has a maximum value 1 and a minimum value 0. In our numerical experiments, the spatial domain $\Omega = [-0.5, 0.5] \times [-0.5, 0.5]$, the center and the deviation of the initial Gaussian are specified as $(x_c, y_c) = (-0.25, 0.0)$ and $\sigma = 0.0447$.

This example has been widely used to evaluate performance of different numerical schemes, such as numerical stability, numerical dispersion, spurious oscillations, deformation, and phase errors as well as other numerical effects arising in porous media fluid flows.

This example was also studied in [20] by using piecewise bilinear finite elements within ELLAM framework. With spatial mesh size $h = 1/64$ and time step $\Delta t = \pi/8$, a maximum value of 0.9987 was

Table 4
Statistics of 2D biorthogonal spline Bior(2, 4) solutions with $\Delta t = \pi/8$

J_c	J_f	Threshold ε	Compr. ratio	Max.	L^∞ error	L^2 error	L^1 error
Exact solution				1	N/A		
7	7	N/A	N/A	1.0050	6.694E − 3	3.647E − 4	4.641E − 5
6	6	N/A	N/A	1.0202	2.015E − 2	9.071E − 4	1.110E − 4
3	6	0	N/A	0.9938	1.641E − 2	8.366E − 4	1.190E − 4
3	6	1E − 4	12.9	0.9938	1.618E − 2	8.522E − 4	1.378E − 4
3	6	5E − 4	20.1	0.9882	1.789E − 2	1.056E − 3	2.006E − 4
3	6	1E − 3	22.3	0.9882	1.905E − 2	1.252E − 3	2.551E − 4
3	6	1E − 2	34.8	1.0625	8.366E − 2	5.593E − 3	9.774E − 4

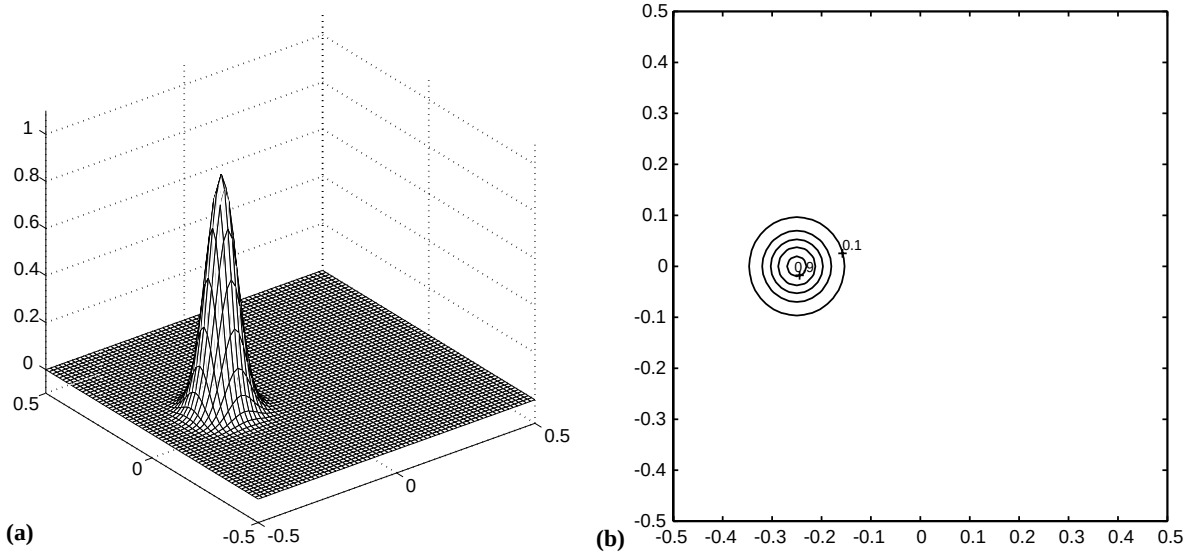

Fig. 4. 2D exact solution at $T = \pi/2$: (a) surface plot; (b) contour interval 0.2.

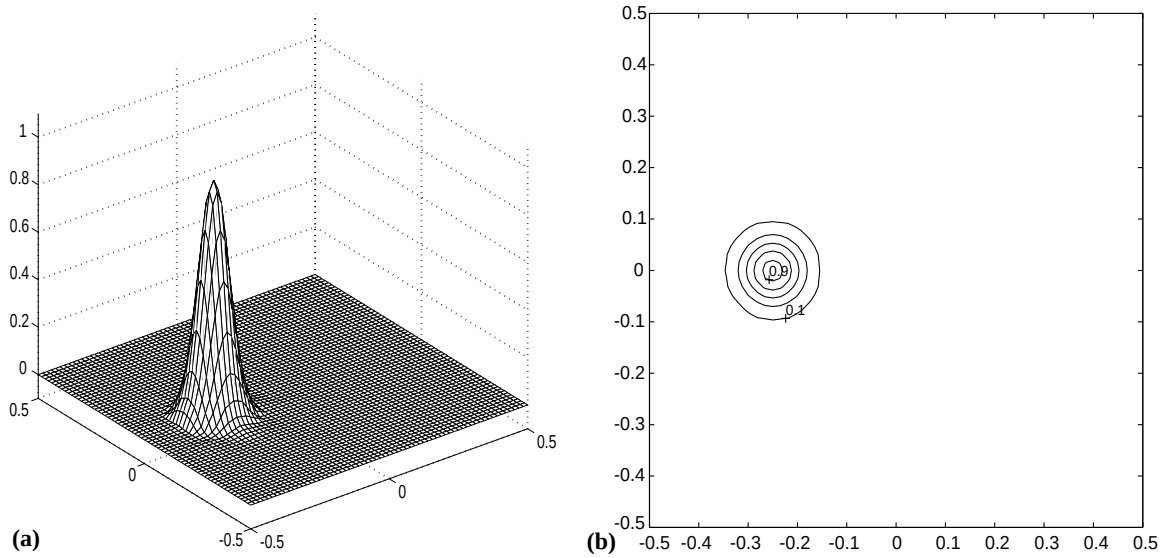

Fig. 5. 2D biorthogonal spline solution at $T = \pi/2$ with threshold 0.0001: (a) surface plot; (b) contour interval 0.2.

obtained for the numerical solution. Here we use the same spatial mesh size ($J_f = 6$ means $h = 1/64$) and the same time step. With compression threshold $\varepsilon = 0.0001$, the biorthogonal spline scheme III generates a numerical solution having maximum value 0.9938. The accuracy of the biorthogonal spline solution is comparable to that of the piecewise bilinear finite element solution, but the compression ratio of the biorthogonal method is as high as 12.9, which means we solve less than a twelfth of the unknowns (see Table 4 and Figs. 4 and 5).

Next we make comparison between the biorthogonal schemes in this paper and the orthogonal schemes proposed in [22]. We take Bior$(2,4)$ for the biorthogonal schemes and the third-order Daubechies wavelet for the orthogonal ones. This should be a fair comparison, since Bior$(2,4)$ primal and dual biorthogonal wavelets and the third-order Daubechies orthogonal wavelet all have the same compact support $[-2,3]$. Thus the same amount of operations is needed for each element in both orthogonal and biorthogonal schemes. From Table 5, we conclude that the biorthogonal schemes perform somewhat better than the

Table 5
Comparison of Bior$(2,4)$ biorthogonal and third-order Daubechies orthogonal schemes for the 2D problem with $\Delta t = \pi/8$

J_c	J_f	Threshold ε	Compr. ratio	Max.	L^∞ error	L^2 error	L^1 error
Bior$(2,4)$ *primals as trial functions, duals as test functions*							
3	6	0	N/A	0.9938	1.641E−2	8.366E−4	1.190E−4
3	6	1E−4	12.9	0.9938	1.618E−2	8.522E−4	1.378E−4
3	6	1E−3	22.3	0.9882	1.905E−2	1.252E−3	2.551E−4
3	6	5E−3	32.7	0.9923	5.956E−2	3.535E−3	6.231E−4
3	6	1E−2	34.8	1.0625	8.366E−2	5.593E−3	9.774E−4
Third-order Daubechies orthogonal wavelets as both trial and test functions							
3	6	0	N/A	0.9919	1.635E−2	9.929E−4	1.465E−4
3	6	1E−4	10.6	0.9895	1.517E−2	1.004E−3	1.659E−4
3	6	1E−3	17.2	0.9877	2.994E−2	1.960E−3	4.047E−4
3	6	5E−3	22.7	1.0275	1.106E−1	6.203E−3	1.248E−3
3	6	1E−2	24.7	0.8980	1.921E−1	1.312E−2	2.552E−3

orthogonal ones, as we expected. For the no-compression multilevel scheme or the compression scheme with small threshold, they both perform very well. But with relatively large thresholds, e.g., $\varepsilon = 0.001, 0.005$, the biorthogonal scheme produces better approximations with even higher compression ratios. Notice that primal biorthogonal wavelets and scaling functions have explicit expressions, for instance, Bior$(2,4)$ primals are just piecewise linear functions. Therefore they are relatively easier to be implemented in programs and therefore take less time in computations.

6. Discussions and summary

First, notice that at each time step, we approximate the solution by a spline. For the initial condition $u_0(\mathbf{x})$, this is equivalent to the nodal interpolation. So it is not necessary to call numerical quadrature to compute the coefficients in the linear combination. This should bring us better approximation to $u_0(\mathbf{x})$ and hence better approximation for the whole solution.

The evaluation of the first term on the right-hand side of (45), (47), or (48) is nonconventional due to the definition of $w(\mathbf{x}, t_{n-1}^+)$, which is obtained via characteristic tracking. To overcome this difficulty, we adopt a backward tracking algorithm. Replacing the dummy variable $\mathbf{x}$ by $\mathbf{x}_*$, we rewrite the term as

$$\int_\Omega U(\mathbf{x}_*, t_{n-1}) w\big(\mathbf{x}_*, t_{n-1}^+\big)\,\mathrm{d}\mathbf{x}_* = \int_\Omega U(\mathbf{x}_*, t_{n-1}) w(\mathbf{x}, t_n) e^{-R(\mathbf{x},t_n)\Delta t_n} \mathbf{J}(\mathbf{x}_*, \mathbf{x})\,\mathrm{d}\mathbf{x}, \tag{65}$$

where $\mathbf{x}_* = \mathbf{y}(t_{n-1}; \mathbf{x}, t_n)$ is obtained by backtracking $(\mathbf{x}, t_n)$ along characteristic to time t_{n-1} and $\mathbf{J}$ is the Jacobian. Note that $w(\mathbf{x}, t_n) = \tilde{\boldsymbol{\Phi}}_{J_f}(\mathbf{x}), \tilde{\boldsymbol{\Phi}}_{J_c}(\mathbf{x})$, or $\tilde{\boldsymbol{\Psi}}^{\mathbf{e}}_{j,\mathbf{k}}(\mathbf{x})$, whose values are available only at dyadic points. Therefore, we apply a composite Simpson or a composite 3rd/5th order Newton–Cotes quadrature on dyadic cells in Ω at time step t_n. All discrete quadrature points $\mathbf{x}_q$ will be dyadic points. Of course, $(\mathbf{x}_q)_* = \mathbf{y}(t_{n-1}; \mathbf{x}_q, t_n)$ are not necessarily dyadic points. But $U((\mathbf{x}_q)_*, t_{n-1})$ can be evaluated explicitly since trial functions are piecewise polynomials (splines). This is also one of the advantages of the biorthogonal spline schemes to the orthogonal wavelet schemes.

The distribution of significant coefficients in (59) might be somewhat irregular after the thresholding process. A naive organization and management of these coefficients could compromise the greatly improved efficiency of the scheme. The tree approximation techniques proposed in [3] give a more efficient organization of the positions of the significant coefficients.

At present stage, we focus on the study of trade-off between compressibility and accuracy. We understand that some optimization of the implementation will fully explore the adaptivity and further improve its performance in CPU time and approximation.

Our numerical results indicate that all three biorthogonal spline schemes are unconditionally stable. Rigorous proofs for these will be presented in our future work.

For initial boundary value problems to advection–reaction equations, biorthogonal spline schemes can also be established by using biorthogonal wavelets on intervals. With the help of ELLAM methodology, we can extend these ideas further to advection-diffusion equations.

In this paper, we present an adaptive biorthogonal spline wavelet ELLAM scheme for multidimensional advection–reaction equations, by incorporating biorthogonal spline wavelet trial and test functions into the framework of the Eulerian–Lagrangian localized adjoint method. The use of the ELLAM framework symmetrizes the governing equation. The symmetric representation of the equation is then solved using MRA and wavelet expansion of trial- and test-spaces. The combination of the ELLAM framework and the biorthogonal wavelets generates unconditionally stable, explicit, adaptive wavelet schemes. The novelty of this work lies in the thresholding schemes used to adaptively reduce the numerical complexity in analogy with wavelet compression of data. Inherent in the scheme is shock-tracking and the packing of the wavelet elements around the feature-detected shocks, followed by the automatic use of coarse elements over smooth

regions and fine wavelet corrections near moving steep fronts. The use of biorthogonal spline wavelets in this paper, rather than the orthogonal scaling functions as proposed in [22], enables us to have explicit representations with a given regularity and to greatly improve the efficiency of the adaptive wavelet schemes.

This class of numerical schemes is promising since it couples the strengths of ELLAM schemes with basis elements that are able to efficiently approximate the solutions in a multiscale framework. In the future we plan to investigate the development of multiresolution lifting schemes for nonuniform (nonlogically rectangular) grids, efficient balance of solution projections into scale and wavelet spaces, efficient treatment of boundary terms, efficient implementation, as well as numerical analysis issues such as stability analysis, convergence analysis, and error estimates.

Acknowledgements

The authors would like to express their sincere thanks to the referees for their very valuable comments and suggestions, which greatly improved the quality of this paper.

References

[1] A. Barinka, T. Barsch, P. Charton, A. Cohen, S. Dahlke, W. Dahmen, K. Urban, Adaptive wavelet schemes for elliptic problems – implementation and numerical experiments, SIAM J. Sci. Comput. 23 (2001) 910.
[2] M.A. Celia, T.F. Russell, I. Herrera, R.E. Ewing, An Eulerian–Lagrangian localized adjoint method for the advection–diffusion equation, Adv. Water Resources 13 (1990) 187.
[3] A. Cohen, W. Dahmen, I. Daubechies, R. DeVore, Tree approximation and optimal encoding, Appl. Comput. Harmon. Anal. 11 (2001) 192.
[4] A. Cohen, W. Dahmen, R. DeVore, Adaptive wavelet methods for elliptic operator equations: convergence rates, Math. Comp. 70 (2001) 27.
[5] A. Cohen, I. Daubechies, J.-C. Feauveau, Biorthogonal bases of compactly supported wavelets, Commun. Pure Appl. Math. 45 (1992) 485.
[6] A. Cohen, S.M. Kaber, S. Müller, M. Postel, Fully adaptive multiresolution finite volume schemes for conservation laws, Math. Comp. 72 (2003) 183.
[7] R. Courant, K.O. Friedrichs, H. Lewy, Uber die partiellen differenzen-gleichungen der mathematisches physik, Mathematische Annalen 100 (1928) 32.
[8] I. Daubechies, Orthogonal bases of compactly supported wavelets, Commun. Pure Appl. Math. 41 (1988) 909.
[9] I. Daubechies, Ten Lectures on Wavelets, SIAM, Philadelphia, 1992.
[10] R.A. DeVore, B. Jawerth, V. Popov, Compression of wavelet decomposition, Am. J. Math. 114 (1992) 737.
[11] A. Haar, Zur theorie der orthogonalen funktionen-systeme, Math. Ann. 69 (1910) 331.
[12] H. Harbrecht, F. Paiva, C. Pérez, R. Schneider, Biorthogonal wavelet approximation for the coupling of FEM–BEM, Numer. Math. 92 (2002) 325.
[13] A. Harten, Multiresolution algorithms for the numerical solution of hyperbolic conservation laws, Commun. Pure Appl. Math. 48 (1995) 1305.
[14] I. Herrera, R.E. Ewing, M.A. Celia, T.F. Russell, Eulerian–Lagrangian localized adjoint methods: the theoretical framework, Numer. Methods PDEs 9 (1993) 431.
[15] P.D. Lax, Hyperbolic Systems of Conservation Laws and the Mathematical Theory of Shock Waves, SIAM, Philadelphia, 1973.
[16] R.J. LeVeque, Numerical Methods for Conservation Laws, Birkhäser, Basel, 1992.
[17] S. Mallat, Multiresolution and wavelet orthonormal bases in $L^2(\mathbb{R})$, Trans. Am. Math. Soc. 315 (1989) 69.
[18] S. Mallat, A Wavelet Tour of Signal Processing, second ed., Academic Press, San Diego, 1999.
[19] Y. Meyer, Wavelets and Operators I, Cambridge University Press, Cambridge, 1992.
[20] H. Wang, R.E. Ewing, G. Qin, S.L. Lyons, M. Al-Lawatia, S. Man, A family of Eulerian–Lagrangian localized adjoint methods for multidimensional advection–reaction equations, J. Comput. Phys. 152 (1999) 120.
[21] H. Wang, R.E. Ewing, T.F. Russell, Eulerian–Lagrangian localized adjoint methods for convection–diffusion equations and their convergence analysis, IMA J. Numer. Anal. 15 (1995) 405.
[22] H. Wang, J. Liu, Development of CFL-free, explicit schemes for multidimensional advection–reaction equations, SIAM J. Sci. Comput. 23 (2001) 1418.